DOI: 10.1021/ma101477s

Macromolecules
ARTICLE

# Following the Synthesis of Metal Nanoparticles within pH-Responsive Microgel Particles by SAXS

**E. Pavlopoulou,[†,‡] G. Portale,[§] K. E. Christodoulakis,[†,‡] M. Vamvakaki,[†,‡] W. Bras,[§] and S. H. Anastasiadis*[,†,⊥]**

[†]*Institute of Electronic Structure and Laser, Foundation for Research and Technology - Hellas, P.O. Box 1527, 711 10 Heraklion Crete, Greece,* [‡]*Department of Materials Science and Technology, University of Crete, 710 03 Heraklion Crete, Greece,* [§]*ESRF, DUBBLE CRG, Netherlands Organization for Scientific Research (NWO), F-38043 Grenoble, France, and* [⊥]*Department of Chemistry, University of Crete, 710 03 Heraklion Crete, Greece*

*Received July 5, 2010; Revised Manuscript Received September 20, 2010*

ABSTRACT: pH-responsive poly(2-(diethylamino)ethyl methacrylate), PDEA, microgels have been utilized as nanoreactors for the formation of metal nanoparticles. The PDEA microgels exhibit reversible swelling properties in water as a function of the solution pH; at low pH, the microgel particles are swollen, while an increase of the pH leads to hydrophobic latex particles. Metal nanoparticles were synthesized within the microgel particles by the incorporation of the appropriate metal precursor followed by metal reduction. Two synthetic routes have been utilized for the preparation of the nanoparticles and are compared herein: in the first method, the $K_2PtCl_6$ precursor was added to the hydrophilic swollen microgel particles at low pH (method A) followed by metal reduction and increase of the pH by the addition of base, while in the second method, $H_2PtCl_6$ was added to the hydrophobic latex particles at high pH and next the metal salt was reduced *in situ* using $NaBH_4$ (method B). The structure of the hybrid systems was investigated by small-angle X-ray scattering (SAXS) during the three steps of the metal nanoparticle synthesis: the original microgel dispersion in water of the appropriate pH, the metal-loaded polymer matrices, and the metal nanoparticle-containing microgels after reduction. The pH-responsive character of the microgels as well as the metal incorporation was confirmed by the scattering profiles. Following metal reduction, Pt nanoparticles are formed with a radius of about 1 nm for both methods. The scattering profiles acquired both before and after reduction for the two methods exhibit differences which are attributed to the spatial distribution of the platinic anions and the Pt nanoparticles.

## I. Introduction

The unique properties of colloidal metal nanoparticles have attracted great interest for their use in catalysis as well as in optical devices, nanoelectronics, and superparamagnetic or ferromagnetic materials.[1−5] However, there is a significant energetic cost associated with their large surface area, and a reduction of their interfacial energy is required to prevent agglomeration. Both inorganic and organic moieties such as small molecule surfactants, functional polymers, zeolite cells, and others have been used to confer nanoparticle stabilization.[6−10]

The incorporation of nanoparticles within polymeric nanostructures has been realized by two different approaches. One approach uses preformed nanoparticles and takes advantage of their cooperative self-organization within the polymer domains.[11−15] The second one involves the *in situ* synthesis of the nanoparticles within the soft matter nanostructures. Functional polymeric materials, e.g., block copolymers,[16−19] dendrimers,[20] and polymer microgels,[21] have attracted particular attention as nanoscopic reaction vessels for growing inorganic metal nanocrystals; reverse micelles formed by small molecule surfactants in organic media[22,23] have been utilized as well. The use of polymers allows potential control of the nanoparticle characteristics and properties by manipulating the molecular structure, the size, and the composition of the macromolecules, whereas it permits utilization of both organic and aqueous dispersing media.

*To whom correspondence should be addressed. E-mail: spiros@iesl.forth.gr.

Responsive microgels are particularly attractive for use in many applications such as protein absorption, immobilization of biomolecules, and drug delivery in the development of sensors and in membrane filtering, while they can be employed as microscopic reactors for the synthesis of inorganic nanoparticles as well.[24−37] Unlike diblock copolymer micelles, which may break apart to the unimer state upon changing the solution conditions, the network structure of the microgel is stable independently of the solution pH, temperature, etc. Moreover, their swelling characteristics can be properly controlled by changes in the external stimuli; such a behavior could be advantageous for a wide range of applications.

Microgel−metal nanoparticle hybrid materials have been prepared by the *in situ* growth of the nanoparticles within the microgel particles.[38−41] Antonietti et al.[24] were the first to report the *in situ* preparation of noble metal colloids within microgel nanoreactors. The effects of the microgel cross-link density and of the concentration of functional groups were investigated and were correlated to the percentage of microgels containing metal nanoparticles. Subsequent studies involved the metalation of microgels comprising a minor fraction of the metal-binding functional groups and a major fraction of nonfunctional moieties.[30,42−44] Kumacheva and co-workers[26,40,45] reported the use of a single class of poly(*N*-isopropylacrylamide-*co*-acrylic acid), P(NIPAM-*co*-AA), microgel templates for the *in situ* production of different types of nanoparticles (semiconductor, metal, and magnetic) and/or nanorods that have led to nanocomposites with unique properties and high structural hierarchy. Suzuki et al.[46,47] showed

 Published on Web 11/12/2010 

that the incorporation of Au and Au/Ag nanoparticles within PNIPAM core−shell particles resulted in hybrid microgels that exhibit thermoreversible color changes. Lu et al.[48,49] reported the modulation of the catalytic activity of Ag nanoparticles incorporated within thermosensitive core−shell particles induced by the thermodynamic phase transition of the carrier networks. Poly(amidoamine) dendrimers with sizes between 3 and 15 nm were incorporated within a poly(hydroxyl ethyl methacrylate) random network by Amis and co-workers;[20,50] metal salts, which either interacted with the dendrimer molecules or diffused within the polymer matrix, were added next followed by metal reduction to produce Au, Pt, or Cu nanoparticles. Small-angle X-ray scattering (SAXS) and transmission electron microscopy (TEM) showed that dendrimer aggregation within the gel was prevented after the addition of the metal salt leading to homogeneous hybrid materials. The use of these nanohybrids as selective nanocatalysts in organic reactions was proposed, whereas the nonlinear optical properties of the Au nanocomposites are attractive for the development of optical devices.

We have recently employed pH-responsive microgels based on poly(2-(diethylamino)ethyl methacrylate), PDEA, as matrices for the formation of nanoparticles at high metal loadings in aqueous media.[51−53] The use of such systems as recoverable catalyst supports in organic chemistry and drug-delivery vehicles has been suggested;[51,54,55] the binding capacity and accessibility of the microgel active sites, the size and number of nanoparticles, and their spatial distribution and degree of dispersion within the polymeric matrix are very important properties for such applications.[56−58] The incorporated metal provides the required contrast and renders SAXS a powerful technique for the characterization of metal-loaded polymeric materials. Amis and co-workers[20,50] have used SAXS to characterize the structure of metalated dendrimers and understand the general features of metal colloid nanotemplating. The size and number density of the metal nanoparticles within each dendrimer were found to depend on the dendrimer generation, while the data supported the presence of a single metal nanoparticle located offset from the center of the dendrimer for G6−G9 dendrimers.[20] The dispersion of the metalated dendrimers within a hydrophilic polymer network was also investigated by SAXS, which showed a uniform dendrimer distribution with the interdendrimer distance being controlled by the dendrimer concentration.[50] Finally, hydrophobically modified dendrimers were studied as monomolecular reverse-micelle systems for the formation of metal nanoparticles within the hydrophilic dendrimer core.[59] SAXS was employed to characterize the nanoscale structure of the dendrimers upon metalation and showed a transition from the spherical monomolecular dendrimers to cylindrical multimolecular assemblies upon loading with the metal salt. The original spherical dendrimer structure was restored following metal reduction to obtain the metal nanocolloids. In a subsequent investigation, Bronstein et al.[60] used anomalous small-angle X-ray scattering to determine the particle size distribution and identify the location of Pt nanoparticles within diblock and triblock copolymer micelles. The metalation of the "soft" polymeric matrix allowed the characterization of the structure of the polymer surrounding the metal colloids as well.

In the present work, the structure of the pH-responsive PDEA microgels is investigated by SAXS before and after metalation as well as the characteristics of the metal nanoparticles synthesized using two different synthetic routes. The structure of the microgel particles is studied during the three steps of the metal nanoparticle synthesis: the dispersions of the original pH-responsive microgels in water, the metal-loaded polymer matrices, and the metal-nanoparticle-containing microgels after reduction. The influence of the metal incorporation method and the metal loading on the metalated microgel nanostructure and on the size and possible spatial distribution of the nanoparticles within the polymeric matrix are examined.

## II. Experimental Section

**Materials.** All chemicals used were commercially available and were purchased from Sigma-Aldrich (Germany). The microgel particles were synthesized in their latex form at pH 9 by emulsion copolymerization of DEA at 70 °C using 1 wt % ethylene glycol dimethacrylate cross-linker, with respect to the monomer, in the presence of monomethoxy-capped poly(ethylene glycol) methacrylate stabilizer ($M_n$ = 2000 g/mol), as described elsewhere.[61] The microgel particles were purified by extensive ultrafiltration to eliminate excess stabilizer as well as traces of unreacted monomer and initiator.

The aqueous solution behavior of the microgel particles was investigated as a function of solution pH by potentiometric titrations at a microgel concentration of 0.1 wt %. The potentiometric titration data (Figure S1, Supporting Information) are used to calculate the effective p$K_a$ of the PDEA microgels as 5.9. Note that the effective p$K_a$ of the PDEA block of a linear diblock copolymer is 6.9.[62]

Moreover, the size of the pH-responsive PDEA microgel particles in water was investigated by dynamic light scattering (DLS; Figure S2, Supporting Information). The wavevector dependence of the scattering intensity leads to the determination of the radii of gyration of the microgels, $R_g$, whereas the measured diffusion coefficients are used to estimate their hydrodynamic radii, $R_h$; $R_g$ and $R_h$ are determined as a function of the solution pH (Table S1, Supporting Information).

**Sample Preparation.** Aqueous dispersions of the PDEA latex particles at concentration 2 wt % were adjusted to the required pH value using 0.1 M HCl or 0.1 M NaOH and were stirred for 24 h before measurement to ensure equilibrium swelling of the microgel particles.

Two different methods were employed for the incorporation of the metal compound within the microgel particles. In the first method (method A), the pH of a 2 wt % aqueous latex dispersion was adjusted to pH 2 by the addition of 0.1 M HCl. The resulting microgel solution was stirred overnight to ensure complete protonation of the tertiary amine groups, and $K_2PtCl_6$ was added next at the appropriate N:Pt molar ratio. The solution was stirred for 24 h to allow for metal complexation to occur, followed by ultrafiltration using a 3 nm pore size filter. Finally, *in situ* metal reduction was carried out using $NaBH_4$, and the pH was increased to ~10 by the addition of 0.1 M NaOH. The sample was stirred overnight followed by ultrafiltration before measurement. In the second method (method B), the metal precursor ($H_2PtCl_6 \cdot 6H_2O$) was added to a 2 wt % aqueous latex suspension at zero effective degree of ionization of the DEA units, $\alpha_{eff}$ = [HCl]/[DEA monomer units], at the required N:Pt molar ratio. The solution was stirred for 24 h, whereas the excess platinic acid was eliminated by ultrafiltration using a 3 nm pore size filter. Finally, metal reduction was carried out using $NaBH_4$, and the samples were stirred for 24 h. All samples were ultrafiltrated before measurement.

The use of $H_2PtCl_6$, instead of its potassium salt, $K_2PtCl_6$, was indeed required in method B (high pH) because the protons derived from the acid dissociation protonate the PDEA amine groups, which become positively charged and, thus, interact via electrostatic interactions with the metal anion complex ($PtCl_6^{2-}$). This leads to the incorporation of the metal within the polymeric matrix in the first step, which is followed by metal reduction to form the metal nanoparticles in the next step. The use of $K_2PtCl_6$ instead of $H_2PtCl_6$ would not give the required proton atoms ($K^+$ will be formed instead) to protonate the tertiary amine groups of the polymer, and thus, metal incorporation would be ineffective[19,53] because metal incorporation in that case proceeds only via N-coordination onto the Pt atom, which is a much slower equilibration process compared to the

quantitative electrostatic complexation that takes place when $H_2PtCl_6$ is used. It is noted that the metal compound $H_2PtCl_6$ was incorporated at a mild pH ~ 8 (zero effective degree of ionization of the DEA monomer repeat units) to avoid the hydrolysis of the metal complex that takes place at high pH which would eventually lead to an ineffective incorporation within the polymer matrix.

**Small-Angle X-ray Scattering.** SAXS experiments were performed on the Dutch-Belgian Beamline (DUBBLE) at the European Synchrotron Radiation Facility (ESRF) station BM26B[63,64] in Grenoble, France. SAXS data were recorded on a two-dimensional position-sensitive detector.[65] Two different energies of the X-ray beam were used, 15 and 8 keV, each one for a different sample-to-detector distance, 2 and 7 m, respectively, and thus, a wide scattering vector range was covered, $0.04 < q < 6.4$ nm$^{-1}$. The magnitude of the scattering vector is $q = (4\pi/\lambda) \sin \theta$, where $2\theta$ is the scattering angle.

The two-dimensional images were radially averaged around the center of the primary beam in order to obtain the isotropic SAXS intensity profiles. The scattering patterns from a specimen of wet collagen (rat tail tendon) and silver behenate were used for the calibration of the wavevector scale of the scattering curves. The data were normalized to the intensity of the incident beam (in order to correct for primary beam intensity fluctuations) and were corrected for absorption, background scattering, and microgel concentration (for the pure microgel solutions). For the metal-containing samples no concentration correction was applied, since the amount of the added metal compound is negligible with respect to the total mass of the sample. Two ionization chambers placed before and after the sample were utilized for monitoring the incident and the transmitted beams. Lupolen and Eltex were used as reference samples for the intensity calibration in absolute units (cm$^{-1}$). The scattering intensity from pure water was subtracted from the total scattering intensity to account for the background correction due to the contribution of density fluctuations. All samples were placed in glass capillary tubes of a diameter of 2 mm, and the measurements were conducted at room temperature (25 °C).

The intensity scattered from a monodisperse collection of particles of volume $V$ and number density $N_p$ is

$$I(q) = N_p(\Delta\rho)^2 V^2 P(q) S(q) \quad (1)$$

where $\Delta\rho$ is the difference in the scattering length densities between the scattering particles and the solvent, $P(q)$ is the form factor of the particles, and $S(q)$ is the structure factor. For very dilute systems, $S(q) \rightarrow 1$ and the structure factor contribution can be neglected. For spherical particles (like the microgel particles of the present work as well as the assumed shape of the metallic nanoparticles), the form factor of a homogeneous sphere of radius $R$ is used:

$$P(q) = \frac{9(\sin qR - qR \cos qR)^2}{(qR)^6} \quad (2)$$

The polydispersity in the particle radius is accounted with a Gaussian distribution $g(r)$

$$g(r) = \frac{1}{\sqrt{2\pi}w} \exp\left(-\frac{(r-R)^2}{2w^2}\right) \quad (3)$$

where $w$ is the standard deviation of the distribution. The scattered intensity, thus, becomes

$$I(q,r) = N_p(\Delta\rho)^2 \int_0^\infty (V(r))^2 P(q,r) g(r)\, dr \quad (4)$$

The calculated intensity is fitted to the experimental data by adjusting the two parameters, $R$ and $w$, and by using a scaling factor related to the product $N_p(\Delta\rho)^2$. The fitting is accomplished by a nonlinear least-squares fitting procedure.

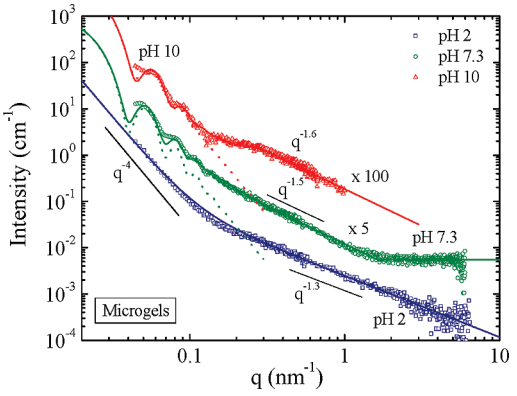


**Figure 1.** Scattering patterns acquired for a 2 wt % PDEA microgel dispersion at pH 2 (open squares), 7.3 (open circles), and 10 (open triangles). The curves for pH 7.3 and pH 10 have been shifted vertically for clarity by multiplying them by 5 and 100, respectively. Solid lines are the respective best fit curves taking into account the scattering contributions discussed in the text. The simulated form factors for the spherical microgels at pH 7.3 and 10 (with the respective polydispersities) are drawn by dotted lines.

When appropriate, different contributions to the scattering from the microgel dispersions are added to eq 4, as will be discussed in the Results section. Moreover, when needed, a constant background type of constant intensity is added at high wavevectors, whose origin is discussed in the text.

## III. Results and Discussion

**Microgel Particles in Water as a Function of Solution pH.** The PDEA microgels exhibit reversible swelling properties in water as a function of the solution pH. At low pH, the microgel particles are swollen due to the protonation of the DEA monomer repeat units, which allows the ingress of water within the microgel particles, whereas the increase of the pH above the effective p$K_a$ value of the microgels leads to the deprotonation of the tertiary amine groups and, thus, to hydrophobic latex particles.[51] Figure 1 shows the scattering patterns acquired for 2 wt % PDEA microgel dispersions at three different pH values of 2, 7.3, and 10. Note that the curves for pH 7.3 and 10 have been shifted vertically for clarity.

The scattered intensity recorded for the microgel dispersion at pH 2 exhibits a $q^{-4}$ dependence in the low wavevector range, while at higher wavevectors it decreases with $q$ as $q^{-1.3}$. The solid line in Figure 1 is the best fit curve obtained by adding these two power-law contributions. The $q^{-4}$ dependence observed in the low $q$-range is attributed to the Porod scattering from the swollen microgel particles at pH 2, whose radius exceeds the length scale accessible within the $q$-range of the present experiment. At pH 2, all DEA units of the microgel are protonated and, thus, the microgels are highly swollen; dynamic light scattering measurements (discussed in the Supporting Information) result in a radius of gyration $R_g = 199$ nm and a hydrodynamic radius $R_h = 200$ nm. On the other hand, the $q^{-1.3}$ power law in the intermediate wavevector range can be attributed to the scattering from the interconnected polymer network within the microgel particle. It is well-known that a network structure scatters as[66,67]

$$S_{fractal}(q) = q^{-f} \quad (5)$$

where $f$ is the fractal dimension ($f < 3$); a fractal dimension close to 1 indicates a loosely connected network, whereas $f$ increases as the network becomes denser. The value of 1.3

estimated for $f$ should be due to the swelling of the microgels at pH 2, which reduces the density of the network.

When the solution pH is raised to 7.3, at least three well-defined minima are observed in the low $q$-range, implying that the radius of the microgel is reduced and now falls within the length scales probed by the present experiment; at pH 7.3, the degree of ionization of the DEA units is estimated as 0.04 by the Henderson−Hasselbalch equation, $\alpha = (1 + 10^{pH-pK_a})^{-1}$. Although the Guinier regime is still not accessible, the positions of the minima are consistent with those of the form factor of a spherical particle (eqs 2−4) and, thus, one can safely derive that the microgel particles are spherical; the spherical shape of the microgels and their narrow size distribution have been confirmed by DLS and TEM in an earlier investigation.[51] The first minimum observed at around 0.069 $nm^{-1}$ is the second-order minimum of the form factor of a sphere with a radius $R = 110$ nm (dotted line in Figure 1), while the sharpness of the minima and the appearance of even the fourth-order minimum are indicative of a narrow particle size distribution. The use of a fractal term $S_{fractal}(q)$, which describes the contribution of the network to the total scattering, eq 5, was required to fit the data for the microgel dispersion at pH 7.3 as well. The best fit curve is presented in Figure 1 and corresponds to the scattering from spherical particles (eq 4), with $R = 110$ nm and $w = 8$ nm (dotted line), plus the scattering from an interconnected polymer network of fractal dimension $f = 1.5$, slightly higher than that found for the swollen microgels at pH 2. These findings confirm that at pH 7.3 the microgel particles are in a more-or-less collapsed state, since $R$ is reduced and the network has become denser.

A similar profile was acquired for the microgel dispersion at pH 10. Analysis of the data results in a mean radius $R = 99$ nm, with an associated standard deviation $w = 11$ nm (dotted line), which can be used as a measure of particle polydispersity, in agreement with dynamic light scattering data that gave a radius of gyration $R_g = 105$ nm and a hydrodynamic radius $R_h = 154$ nm (see Supporting Information). Moreover, $f$ was found to be 1.6, close to the value obtained at pH 7.3. These findings indicate a further collapse of the microgel particle as the pH increases further above the effective $pK_a$ (5.9) of the DEA repeat units in the PDEA microgels.[53]

**Metalation of the Microgel Particles Using Method A.** Figure 2 shows the SAXS profiles acquired for the three synthetic steps followed for the formation of the Pt nanoparticles within the PDEA microgels using method A at a N:Pt=4:1 molar ratio. Method A involves the metalation of the hydrophilic microgel particles at low pH using $K_2PtCl_6$ and the subsequent *in situ* metal reduction using $NaBH_4$, followed by the increase of the pH to 10 by the addition of NaOH.

As discussed in the previous section, the microgel particles at pH 2 (first step in Figure 2) are in the swollen state with a fractal dimension $f = 1.3$ and a diameter that exceeds the length scale accessible within this experiment. After the incorporation of the metal precursor, the scattered intensity increases abruptly due to the increase of the contrast induced by the presence of the metal species within the microgel particle (second step in Figure 2). The increase in the scattered intensity is more pronounced in the low wavevector range, where a $q^{-4}$ dependence is still observed and is attributed to the scattering from the metalated microgel particles.[68]

Moreover, besides the fractal contribution to the scattering from the interconnected network, a shoulder appears at around $q = 0.4$ $nm^{-1}$ and ends at a background of constant

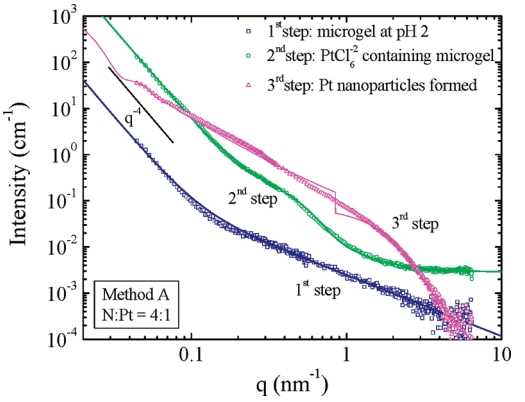


**Figure 2.** Scattering intensity curves acquired for the various synthetic steps followed for the synthesis of Pt nanoparticles within the PDEA microgels using method A at a 4:1 N:Pt molar ratio. Open squares: microgel at pH 2. Open circles: microgel after $PtCl_6^{2-}$ complexation. Open triangles: microgel following metal salt complexation and reduction. Solid lines are the respective best fit curves taking into account the scattering contributions discussed in the text.

intensity. The shoulder indicates the presence of small entities of different scattering contrast, which can be attributed to the aggregation of ion-neutralized hydrophobic polymer within the hydrophilic microgel network. This suggests that the incorporated platinum anions are not homogeneously dispersed within the microgel particles; the $PtCl_6^{2-}$ anions are localized in these neutralized and, thus, hydrophobic regions, which would possibly serve as the nucleation sites for the formation of the platinum nanoparticles upon metal reduction (third step in Figure 2, to be discussed later). For the analysis presented below it is assumed that these hydrophobic regions are spherical.

The experimental scattering curve is fitted to that calculated by the summation of a $q^{-4}$ power law, a fractal term $S_{fractal}(q)$, eq 5, and the form factor of a spherical domain

$$I(q) = Aq^{-4} + Bq^{-f} + N_p(\Delta\rho)^2 \int_0^\infty (V(r))^2 P(q,r) f(r)\, dr \quad (6)$$

attributed to the contribution of the large microgel particle ($q^{-4}$), which is too large to be seen within the present $q$ range, the interconnected network ($q^{-f}$), and the hydrophobic domains. It is noted that the possible interference terms in the scattering intensity of complicated particles, such as the microgels investigated in this work, can be neglected in this case because of the large difference in the size of the microgels compared to that of the small hydrophobic regions.[69] Despite the large polydispersity, the radius of these hydrophobic domains is estimated to be ~3 nm, while the fractal dimension is estimated as $f = 1.6$, which is similar to that derived for the pure microgel particles at pH 10, verifying the collapse of the swollen microgels upon metal complexation.[51]

The polymer-to-metal mole ratio was varied to investigate the effect of the metal loading on the microgel structure and the characteristics of the metal nanoparticles formed after metal reduction. The scattering profiles acquired for the three $K_2PtCl_6$-loaded microgel samples studied in this work are presented in Figure 3, along with the corresponding best fit curves. At a low metal loading (N:Pt = 8:1 molar ratio) the shape of the SAXS pattern is similar to that of the pure microgel solution at pH 2 for low and intermediate wavevectors, whereas it is shifted to higher intensities, indicating that the metal anions are bound within the microgel particles

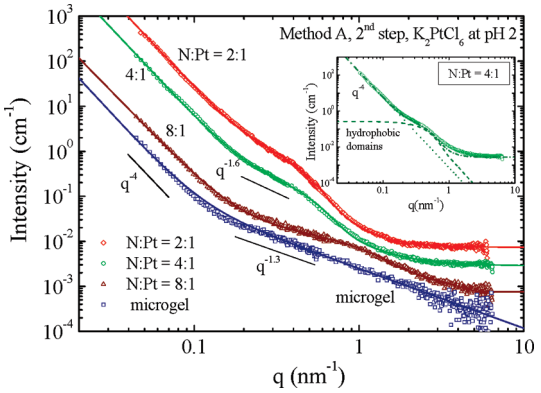


**Figure 3.** Scattering intensity profiles acquired for the $K_2PtCl_6$-loaded microgels at 2:1 (open diamonds), 4:1 (open circles), and 8:1 (open triangles) N:Pt metal loading together with the microgel particle at pH 2 (open squares). Solid lines are the respective best fit curves taking into account the scattering contributions discussed in the text. The individual contributions to the scattering of the large microgel and of the metal-neutralized hydrophobic domains are separately shown in the inset for the N:Pt = 4:1 metal loading.

and increase the contrast between the particle and the aqueous medium. The $q^{-1.3}$ dependence is again evident in the intermediate $q$-range, implying that the density of the network is almost not affected by the presence of the metal anions at this very low metal loading. A bump is also evident at $q \sim 1$ nm$^{-1}$ similar to that discussed above (second step in Figure 2); analysis of the scattering data using eq 6 results in a size of the hydrophobic domains of ~1−2 nm. The expected decrease in the microgel size and the increase in the density of the network are very small[52] and, thus, cannot be probed by SAXS. By increasing the metal loading to N:Pt = 4:1 molar ratio, the scattering curve is shifted to even higher intensities, due to the increase of the $PtCl_6^{2-}$ content, whereas the presence of hydrophobic neutralized regions within the microgels is evident, as discussed for Figure 2. The individual contributions to the scattering of the large microgel and of the metal-neutralized hydrophobic domains are separately shown in the inset of Figure 3 for the N:Pt = 4:1 system. At the same time, the microgels collapse and the network becomes denser, as indicated by the higher estimated fractal dimension ($f = 1.6$). Similar results were obtained for the microgel loaded at a N:Pt = 2:1 molar ratio; the use of eq 6 to fit the scattering curve gave a radius of around 4 nm for the hydrophobic neutralized regions along with a fractal dimension $f = 1.6$ for the collapsed dense network. It is noted that the fractal dimension increases from ~1.3 at 8:1 metal loading to ~1.6 for the high metal loadings 4:1 and 2:1, suggesting that the network becomes denser upon metal complexation. The shrinkage of the microgel particles should result in the appearance of form factor minima in the low $q$-range of the scattering profiles; however, the increased effective polydispersity due to possibly nonuniform metalation of all the particles or the increase in the intensity scattered by the metalated network prevents the observation of such form factor minima.

Additionally, a gradual increase of the background intensity at high wavevectors is observed as the metal loading increases. Since the background intensity results from the sum of the scattering from the atomic species that do not participate in the scattering objects, which have been accounted for, this gradual increase is attributed to the distribution of metal anions over the whole volume of the microgel particles; note that the unbound anions were removed from the solution by ultrafiltration. These results suggest that the metalation of the microgels utilizing method A leads to a distribution of the $PtCl_6^{2-}$ anions within the whole polymeric particle, causing a gradual increase in the network density as the metal loading increases. More interestingly, local metal-neutralized hydrophobic domains are formed, where the metal nanoparticles may nucleate in the next synthetic step.

After metal reduction, the scattering profile is significantly altered (third step in Figure 2). The intensity increases in the high wavevector range, signifying the presence of very small particles. On the other hand, the intensity in the low wavevector range decreases compared to that of the $PtCl_6^{2-}$ containing microgel. These results suggest a redistribution of the scattering mass: before reduction, the Pt anions were distributed all over the microgel particle, resulting in high intensity at low wavevectors while, after reduction, platinum nanoparticles are formed embedded within the polymer network, which scatter at higher wavevectors.

The scattering patterns acquired for the nanoparticle impregnated microgels at the three polymer-to-metal ratios studied in this work are shown in Figure 4. The shapes of the profiles are similar for all three samples while the total scattering intensity increases with the metal loading in the microgel. The profile that corresponds to the N:Pt = 2:1 molar ratio exhibits two shallow minima in the low wavevector range, which allow to estimate the size of the microgel $R$ to be around 117 nm; it should be reminded that the shape of the nanoparticle-containing microgels remained spherical, as proved by DLS and TEM measurements.[51] The data in the high wavevector range can be fitted with the form factor of spherical particles with a radius of 0.8 nm and a polydispersity of around 0.3 nm, which are attributed to the metal nanocrystals embedded within the microgels. The simulated contributions of the microgel particles ($R = 117$ nm; 10% size polydispersity) and the metal nanoparticles to the total scattering for the 2:1 N:Pt loading are presented in the inset as is the sum of these two contributions. In order to fit the data at intermediate wavevectors, the incorporation of a fractal term, $q^{-f}$, was required. The value obtained for the fractal dimension was $f = 2$, somehow higher than that obtained for the pure microgels in the collapsed state, possibly because of distortions of the network by the presence of the metal nanoparticles. It is noted that a high-wavevector cutoff was used for the fractal contribution to the scattering since the expression $q^{-f}$ is valid for wavevectors lower than those corresponding to the mesh size of the network, which is estimated as 7−8 nm for the microgels with 1% cross-link density. The sum of the contributions of the polydisperse Pt nanoparticles, the spherical microgel particle, and the interconnected network is shown in Figure 4 as a solid line. Note that it is the use of a cutoff wavevector together with the fact that cross-correlation terms were not used in the scattering intensity calculation that results in the appearance of a steplike feature in the calculated scattering curve. The scattering intensity in the intermediate range should in principle include contributions from interference terms introduced in the scattering of complex particles due to the cross-correlation either between the particles and the network or between the nanoparticles themselves. However, it was decided to avoid using empirical interference terms since these cross-correlations were well beyond the focus of the present article.

Similar analysis was applied to the scattering profile acquired for the metal-containing microgel particles at a 4:1 metal loading after reduction (third step in Figure 2 and Figure 4). The radius of the microgel particles was found to be around 120 nm, suggesting again the collapse of the

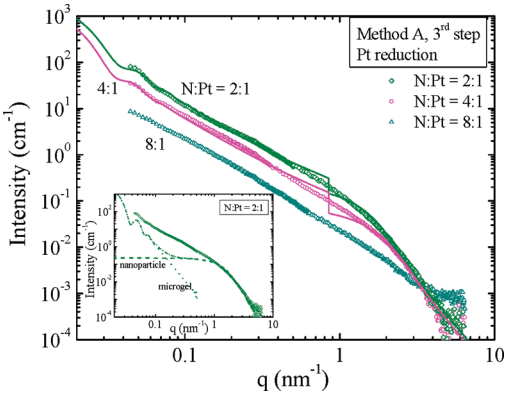


**Figure 4.** Scattering intensity profiles of the Pt nanoparticle-containing PDEA microgels, obtained after reduction of the $K_2PtCl_6$-loaded microgels at a 2:1 (open diamonds), 4:1 (open circles), and 8:1 (open triangles) N:Pt molar ratio. Solid lines are the respective best fit curves taking into account the scattering contributions discussed in the text. The contributions of the microgel (dotted line) and the metal nanoparticles (dashed line) to the total scattered intensity are presented in the inset for the 2:1 N:Pt metal loading together with the sum of these two contributions. High-wavevector cutoffs of 0.85 $nm^{-1}$ were used for the fractal contribution for the 4:1 and 2:1 samples (see text).

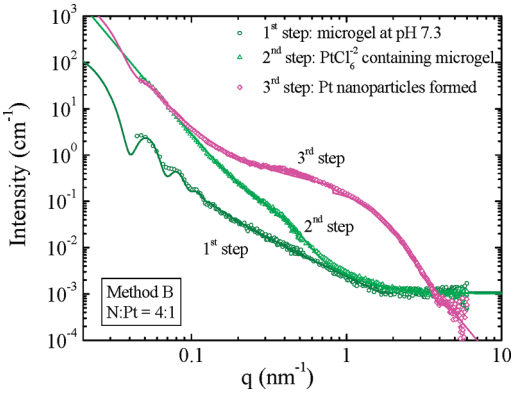


**Figure 5.** Scattering intensity profiles acquired for the various synthetic steps followed for the formation of Pt nanoparticles within the PDEA microgels using method B at a 4:1 N:Pt molar ratio. Open circles: microgel at pH 7.3; open triangles: microgel after $H_2PtCl_6$ incorporation; open diamonds: microgel following metal loading and reduction. Solid lines are the respective best fit curves taking into account the scattering contributions discussed in the text.

microgels, while polydisperse Pt nanoparticles with a mean radius of ~0.7 nm were formed. Moreover, analysis of the data required the use of a fractal term with $f = 1.9$, indicating again a distorted network. For the N:Pt = 8:1 metal loading the shape of the curve is similar (Figure 4), implying that the sample comprises similar structural components. In the high $q$-range a nanoparticle radius of around 0.7 nm was derived with a very high polydispersity; however, the size of the microgels could not be calculated because no minima were evident in the low $q$ range; this is why no fitted curve is shown for N:Pt = 8:1.

Thus, one can conclude that polydisperse metal nanoparticles are formed within the microgel particles in all cases, while the metal loading does not affect significantly the size of the nanoparticles, which is almost constant with a radius of around 1 nm. Yet, the increase of the intensity at low wavevecrors when increasing the metal loading (decreasing the N:Pt ratio) reveals that the number of nanoparticles formed within the microgels increases with the metal loading. At higher metal loadings the number of nucleation sites increases, while the growth of the nanoparticles, which is dictated mainly by thermodynamic terms, remains constant, leading to nanoparticles of similar size. At the same time, it is found that the fractal term contribution required a fractal exponent $f$ higher than that of the collapsed network, thus, providing evidence that the network is distorted by the presence of the nanoparticles. The latter is a very strong indication that indeed the nanoparticles are formed within the microgel particles and is the first direct proof for the spatial location of the nanoparticles since all characterization techniques used previously could not provide this information.

**Metalation of the Microgel Particles Using Method B.** The structure of the metalated samples using method B, which involves the incorporation of the metal-containing acid precursor, $H_2PtCl_6$, into the hydrophobic latex particles at zero effective degree of ionization of the PDEA units, followed by *in situ* metal reduction, was investigated as well. Two polymer-to-metal molar ratios, N:Pt = 4:1 and 16:1, were studied. As discussed above, the microgel particles are in the collapsed state at high pH. For pH 7.3 and 10, the radii were found to be 110 and 99 nm, respectively, while the fractal dimension was 1.6, suggesting an increase of the density of the network (Figure 1).

Figure 5 presents the SAXS profiles acquired for the various synthetic steps followed for the synthesis of Pt nanoparticles within the PDEA microgels at pH 7.3 and a N:Pt = 4:1 molar ratio. The scattering from the dispersion of the microgels at pH 7.3 was discussed in relation to Figure 1 earlier. Addition of the metal precursor to this dispersion leads to an abrupt increase of the scattered intensity at low wavevectors, which is attributed to the metal incorporation within the polymeric matrix and the increase in the excess electron density. For high wavevectors ($q > 1$ $nm^{-1}$), the intensity drops to that obtained for the pure microgel solution.

The scattering intensity profiles of the $H_2PtCl_6$-loaded microgels are shown in Figure 6 along with the corresponding best fit curves for two different metal loadings. A shoulder similar to that observed for the scattering profiles of the $K_2PtCl_6$-loaded particles of method A is observed, and thus, the experimental curves were fitted using eq 6 to take into account the $q^{-4}$ contribution from the microgel particles, the fractal term $S_{fractal}(q)$ that describes the network scattering, and the form factor of a spherical particle for the metal-neutralized hydrophobic domains. Although the high pH value suggests that the microgel particles should be collapsed, no form factor minima are apparent in the low wavevector regime due to the broadening of the external surface of the particles. Metalated hydrophobic regions of around 5 nm in radius were formed within the particles when loaded at N:Pt = 4:1 molar ratio, and the fractal dimension estimated from the intermediate $q$-range data was $f = 1.6$, indicating a collapsed network as discussed above. The individual contributions to the scattering of the large microgel and of the metal-neutralized hydrophobic domains are separately shown in the inset of Figure 6 for the N:Pt = 4:1 system. For the N:Pt = 16:1 sample, the corresponding values were 2.5 nm for the metalated hydrophobic domains and $f = 1.5$ for the fractal dimension. In contrast to method A, the background intensity is independent of the metal loading and is similar to that obtained for the pure microgel dispersion. This suggests that the $PtCl_6^{2-}$ anions are locally confined within the microgel particles and are not distributed over the whole volume of the microgel, as found for method A.

The differences in the distribution of the incorporated metal species observed for the two methods is due to the different processes that take place during metalation. The

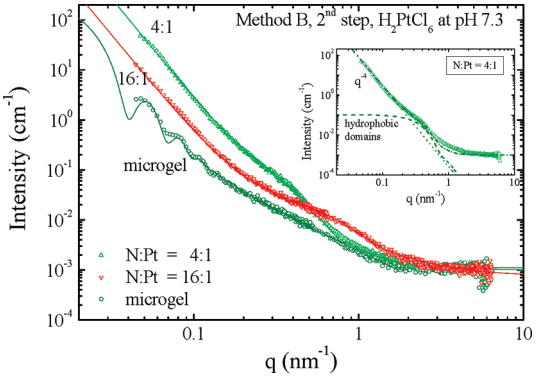


**Figure 6.** Scattering intensity profiles acquired for the microgels loaded with $H_2PtCl_6$ at pH 7.3 for 4:1 (open triangles) and 16:1 (open inverted triangles) N:Pt molar ratio together with the pure microgel at pH 7.3 (open circles). Solid lines are the respective best fit curves taking into account the scattering contributions discussed in the text. The individual contributions to the scattering of the large microgel and of the metal-neutralized hydrophobic domains are separately shown in the inset for the N:Pt = 4:1 metal loading.

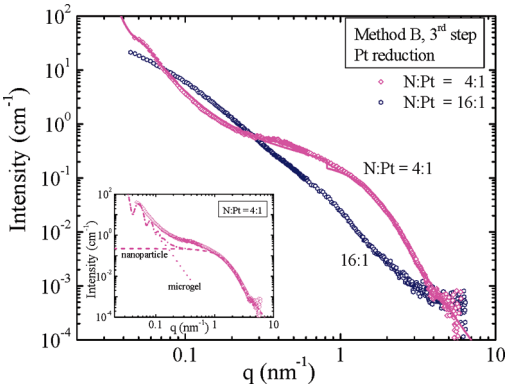


**Figure 7.** Scattering intensity profiles of the Pt nanoparticle-containing PDEA microgels, obtained after reduction of the $H_2PtCl_6$-loaded microgels (method B) at a 4:1 (open diamonds) and 16:1 (open hexagons) N:Pt molar ratio. The solid line is the best fit curve for the 4:1 N:Pt loading taking into account the scattering contributions discussed in the text. The contributions of the microgel (dotted line) and the metal nanoparticles (dashed line) to the total scattered intensity are presented in the inset for the 4:1 N:Pt metal loading together with the sum of these two contributions. A high-wavevector cutoff of 0.85 $nm^{-1}$ was used for the fractal contribution to the scattering for the 4:1 sample (see text).

metal incorporation in method A occurs in one step, which consists of the ionic complexation of the anionic metal species by the cationic polymer due to electrostatic interactions over the whole volume of the particle. In method B, the hexachloroplatinic acid added to the microgel dispersion at pH 7.3 partially protonates the tertiary amine groups of the microgels and induces a local swelling of the microgel. Subsequently, the cationic amine groups formed complex the divalent metal anions leading to the metalated hydrophobic nanodomains.

Following metal reduction, the formation of Pt nanoparticles is manifested by the significant increase of the scattered intensity in the high wavevector range (Figure 5). The SAXS profiles acquired following metal reduction of the $H_2PtCl_6$-loaded microgels are presented in Figure 7 for two different metal loadings. In order to fit the data, a similar procedure to that used for the $K_2PtCl_6$-loaded microgels was applied (inset for N:Pt = 4:1). The radius of the metal nanoparticles formed within the PDEA microgels was calculated to be around 1 nm with a standard deviation of around 0.30 nm, while larger particles with radius estimated as ~2 nm were formed for the N:Pt = 16:1 loading. Note that the high-wavevector cutoff used for the fractal contribution leads to the appearance of the weak step in the calculated scattering curve since again the contribution of interference terms was not included in the calculations. The simulated contributions of the microgel particles ($R = 109$ nm, 10% size polydispersity) and the metal nanoparticles to the total scattering are presented in the inset for the N:Pt = 4:1 metal loading as is the sum of these two contributions; the need of a contribution due to the fractal term is evident. For both metal loadings, the increased intensity in the low wavevector range, with respect to that of the pure microgel (Figure 5), indicates the successful impregnation of the polymeric matrices with the Pt particles. The radius of the metal nanoparticles was found to decrease with increasing metal loading, unlike method A. The fitted fractal dimension $f$ is estimated to be 1.6 for both samples, equal to that obtained for the network of the pure microgel at the collapsed state indicating that the network is not appreciably distorted by the presence of the metal nanoparticles in contrast to the behavior found for method A. One could speculate that this may suggest that the metal nanoparticles are not distributed within the whole volume of the microgel particles. A possible scenario is the metalation of only an outer shell of the microgels, which would lead to the formation of shell-decorated microgel particles and a large nonmetalated microgel core; however, the scattering profiles for the metal-containing microgels (Figure 6) do not require the use of a core−shell type of form factor for their analysis.

## IV. Concluding Remarks

SAXS has been used to investigate the structure of pH-responsive microgels before and after metal incorporation. The decrease in the microgel radius accompanied by an increase of the fractal dimension $f$ when increasing the solution pH confirmed the pH-responsive character of the microgels. These tertiary-amine-based PDEA microgels were utilized as nanoreactors for the formation of Pt nanoparticles. Two synthetic routes have been used for the incorporation of the metal precursor; in the first method, the $K_2PtCl_6$ precursor was added to the hydrophilic swollen microgel particles at low pH followed by metal reduction and an increase of the pH with NaOH (method A), while in the second method, $H_2PtCl_6$ was added to the hydrophobic latex particles at high pH, followed by *in situ* metal reduction (method B). The structure of the metalated particles was investigated by SAXS during the three steps of the metal nanoparticle synthesis: the original polymer dispersions in water, the metal-loaded polymer matrices, and the metal-nanoparticle-containing microgels after reduction. The influence of the metal loading on the structure of the microgels and the characteristics of the nanoparticles was examined.

The addition of the metal precursor resulted in an increase of the scattered intensity at low wavevectors for both methods, signifying the complexation of the platinic salt by the polymeric matrix. The increase of the scattering intensity observed in the intermediate wavevector range suggested that the metal compound is not homogeneously distributed within the metalated volume and evidenced the formation of neutralized and, thus, hydrophobic polymer−metal domains. However, further analysis of the scattering patterns indicated that, in method A, isolated $PtCl_6^{2-}$ anions were also distributed within the whole volume of the microgel particle, while only local metalated polymer nanodomains were apparent in method B. Following metal reduction, Pt nanoparticles were formed. The size of these nanoparticles was found to be around 1−2 nm in diameter

independent of the metal loading and the method used, suggesting an increase in the number of nanoparticles formed within the polymer microgels when increasing the metal loading. On the other hand, an important difference concerning the topology of the polymer network within the microgel arises for the two methods: a distorted network is found for the nanoparticle-containing microgel particles of method A suggesting microgels homogeneously impregnated with Pt nanoparticles, while the nondistorted collapsed network of method B suggests a non-homogeneous distribution of nanoparticles within the microgels.

**Acknowledgment.** We acknowledge that part of this research was sponsored by NATO Scientific Affairs Division (Science for Peace Programme, projects SfP-981438 and SfP-974173), the Greek General Secretariat of Research and Technology (PENED 2003 Programme, project 03EΔ581), and the European Union (NMP3-CT-2005-506621 and NMP3-SL-2008-214095). The Netherlands Organisation for Scientific Research (NWO) and ESRF are acknowledged for granting the beamtime, and Giuseppe Portale is grateful to the Dutch Polymer Institute (DPI) for funding.

**Supporting Information Available:** Figures S1 and S2 and Table S1. This material is available free of charge via the Internet at http://pubs.acs.org.

## References and Notes

(1) Henglein, A. *Chem. Rev.* **1989**, *89*, 1861–1873.
(2) Lewis, L. N. *Chem. Rev.* **1993**, *93*, 2693–2730.
(3) Feldheim, D. L.; Grabar, K. C.; Natan, M. J.; Mallouk, T. E. *J. Am. Chem. Soc.* **1996**, *118*, 7640–7641.
(4) Haruta, M. *Catal. Today* **1997**, *36*, 153–166.
(5) Jaramillo, T. F.; Baeck, S. H.; Cuenya, B. R.; McFarland, E. W. *J. Am. Chem. Soc.* **2003**, *125*, 7148–7149.
(6) Chan, Y. N. C.; Craig, G. S. W.; Schrock, R. R.; Cohen, R. E. *Chem. Mater.* **1992**, *4*, 885–894.
(7) Papisov, I. M.; Yablokov, Y. S.; Prokof'ev, A. I. *Polym. Sci., Ser. A* **1994**, *36*, 291.
(8) Schmidt, G. *Clusters and Colloids*; Wiley-VCH: Weinheim, 1994.
(9) Antonietti, M.; Wenz, E.; Bronstein, L.; Seregina, M. *Adv. Mater.* **1995**, *7*, 1000–1005.
(10) Pileni, M. P. *Langmuir* **1997**, *13*, 3266–3276.
(11) Bockstaller, M. R.; Lapetnikov, Y.; Margel, S.; Thomas, E. L. *J. Am. Chem. Soc.* **2003**, *125*, 5276–5277.
(12) Chiu, J. J.; Kim, B. J.; Kramer, E. J.; Pine, D. J. *J. Am. Chem. Soc.* **2005**, *127*, 5036–5037.
(13) Bockstaller, M. R.; Mickiewicz, R. A.; Thomas, E. L. *Adv. Mater.* **2005**, *17*, 1331–1349.
(14) Lin, Y.; Boker, A.; He, J.; Sill, K.; Xiang, H.; Abetz, C.; Li, X.; Wang, J.; Emrick, T.; Long, S.; Wang, Q.; Balazs, A.; Russell, T. P. *Nature* **2005**, *434*, 55–59.
(15) Balazs, A. C.; Emrick, T.; Russell, T. P. *Science* **2006**, *314*, 1107–1110.
(16) Chernyshov, D. M.; Bronstein, L. M.; Borner, H.; Berton, B.; Antonietti, M. *Chem. Mater.* **2000**, *12*, 114–121.
(17) Spatz, J. P.; Mossmer, S.; Hartmann, C.; Moller, M.; Herzog, T.; Krieger, M.; Boyen, H. G.; Ziemann, P.; Kabius, B. *Langmuir* **2000**, *16*, 407–415.
(18) Vamvakaki, M.; Papoutsakis, L.; Katsamanis, V.; Afchoudia, T.; Fragouli, P. G.; Iatrou, H.; Hadjichristidis, N.; Armes, S. P.; Sidorov, S.; Zhirov, D.; Zhirov, V.; Kostylev, M.; Bronstein, L. M.; Anastasiadis, S. H. *Faraday Discuss.* **2005**, *128*, 129–147.
(19) Bronstein, L. M.; Vamvakaki, M.; Kostylev, M.; Katsamanis, V.; Stein, B.; Anastasiadis, S. H. *Langmuir* **2005**, *21*, 9747–9755.
(20) Gröhn, F.; Bauer, B. J.; Akpalu, Y. A.; Jackson, C. L.; Amis, E. J. *Macromolecules* **2000**, *33*, 6042–6050.
(21) Pich, A.; Bhattacharya, S.; Lu, Y.; Boyko, V.; Adler, H. A. P. *Langmuir* **2004**, *20*, 10706–10711.
(22) Petit, C.; Pileni, M. P. *J. Phys. Chem.* **1988**, *92*, 2282–2286.
(23) Lisiecki, I.; Pileni, M. P. *Langmuir* **2003**, *19*, 9486–9489.
(24) Antonietti, M.; Gröhn, F.; Hartmann, J.; Bronstein, L. *Angew. Chem., Int. Ed. Engl.* **1997**, *36*, 2080–2083.
(25) Pardo-Yissar, V.; Gabai, R.; Shipway, A. N.; Bourenko, T.; Willner, I. *Adv. Mater.* **2001**, *13*, 1320–1323.
(26) Xu, S.; Zhang, J.; Paquet, C.; Lin, Y.; Kumacheva, E. *Adv. Funct. Mater.* **2003**, *13*, 468–472.
(27) Pardo-Yissar, V.; Bourenko, T.; Wasserman, J.; Willner, I. *Adv. Mater.* **2002**, *14*, 670–673.
(28) Gattas-Asfura, K. M.; Zheng, Y.; Micic, M.; Snedaker, M. J.; Ji, X.; Sui, G.; Orbulescu, J.; Andreopoulos, F. M.; Pham, S. M.; Wang, C.; Leblanc, R. M. *J. Phys. Chem. B* **2003**, *107*, 10464–10469.
(29) Jones, C. D.; Serpe, M. J.; Schroeder, L.; Lyon, L. A. *J. Am. Chem. Soc.* **2003**, *125*, 5292–5293.
(30) Biffis, A.; Orlandi, N.; Corain, B. *Adv. Mater.* **2003**, *15*, 1551–1555.
(31) Murthy, N.; Xu, M.; Schuck, S.; Kunisawa, J.; Shastri, N.; Fréchet, J. M. J. *Proc. Natl. Acad. Sci. U.S.A.* **2003**, *100*, 4995–5000.
(32) Cao, R.; Gu, Z.; Patterson, G. D.; Armitage, B. A. *J. Am. Chem. Soc.* **2003**, *126*, 726–727.
(33) Motornov, M.; Roiter, Y.; Tokarev, I.; Minko, S. *Prog. Polym. Sci.* **2010**, *35*, 174–211.
(34) Akamatsu, K.; Shimada, M.; Tsuruoka, T.; Nawafune, H.; Fujii, S.; Nakamura, Y. *Langmuir* **2009**, *26*, 1254–1259.
(35) Wu, W.; Zhou, T.; Zhou, S. *Chem. Mater.* **2009**, *21*, 2851–2861.
(36) Agrawal, M.; Pich, A.; Gupta, S.; Zafeiropoulos, N. E.; Rubio-Retama, J.; Simon, F.; Stamm, M. *J. Mater. Chem.* **2008**, *18*, 2581–2586.
(37) Howse, J. R.; Topham, P.; Crook, C. J.; Gleeson, A. J.; Bras, W.; Jones, R. A. L.; Ryan, A. J. *Nano Lett.* **2006**, *6*, 73–77.
(38) Xu, X.; Majetich, S. A.; Asher, S. A. *J. Am. Chem. Soc.* **2002**, *124*, 13864–13868.
(39) Kim, J.-H.; Lee, T. R. *Chem. Mater.* **2004**, *16*, 3647–3651.
(40) Gorelikov, I.; Field, L. M.; Kumacheva, E. *J. Am. Chem. Soc.* **2004**, *126*, 15938–15939.
(41) Gong, Y.; Gao, M.; Wang, D.; Mohwald, H. *Chem. Mater.* **2005**, *17*, 2648–2653.
(42) Martinez-Rubio, M. I.; Ireland, T. G.; Fern, G. R.; Silver, J.; Snowden, M. J. *Langmuir* **2001**, *17*, 7145–7149.
(43) Zhang, J.; Coombs, N.; Kumacheva, E.; Lin, Y.; Sargent, E. H. *Adv. Mater.* **2002**, *14*, 1756–1759.
(44) Pich, A.; Hain, J.; Lu, Y.; Boyko, V.; Prots, Y.; Adler, H.-J. *Macromolecules* **2005**, *38*, 6610–6619.
(45) Zhang, J.; Xu, S.; Kumacheva, E. *J. Am. Chem. Soc.* **2004**, *126*, 7908–7914.
(46) Suzuki, D.; Kawaguchi, H. *Langmuir* **2005**, *21*, 8175–8179.
(47) Suzuki, D.; Kawaguchi, H. *Langmuir* **2006**, *22*, 3818–3822.
(48) Lu, Y.; Mei, Y.; Drechsler, M.; Ballauff, M. *Angew. Chem., Int. Ed.* **2006**, *45*, 813–816.
(49) Lu, Y.; Mei, Y.; Ballauff, M.; Drechsler, M. *J. Phys. Chem. B* **2006**, *110*, 3930–3937.
(50) Gröhn, F.; Kim, G.; Bauer, B. J.; Amis, E. J. *Macromolecules* **2001**, *34*, 2179–2185.
(51) Palioura, D.; Armes, S. P.; Anastasiadis, S. H.; Vamvakaki, M. *Langmuir* **2007**, *23*, 5761–5768.
(52) Anastasiadis, S. H.; Vamvakaki, M. *Int. J. Nanotechnol.* **2009**, *6*, 46–70.
(53) Christodoulakis, K. E.; Palioura, D.; Anastasiadis, S. H.; Vamvakaki, M. *Top. Catal.* **2009**, *52*, 394–411.
(54) Dickerson, T. J.; Reed, N. N.; Janda, K. D. *Chem. Rev.* **2002**, *102*, 3325–3344.
(55) Pardini, O. R.; Amalvy, J. I.; François, N.; Daraio, M. E. *J. Appl. Polym. Sci.* **2007**, *104*, 4035–4040.
(56) Eichenbaum, G. M.; Kiser, P. F.; Shah, D.; Meuer, W. P.; Needham, D.; Simon, S. A. *Macromolecules* **2000**, *33*, 4087–4093.
(57) Peng, S.; Wu, C. *J. Phys. Chem. B* **2001**, *105*, 2331–2335.
(58) Amigoni-Gerbier, S.; Desert, S.; Gulik-Kryswicki, T.; Larpent, C. *Macromolecules* **2002**, *35*, 1644–1650.
(59) Gröhn, F.; Bauer, B. J.; Amis, E. J. *Macromolecules* **2001**, *34*, 6701–6707.
(60) Bronstein, L. M.; Sidorov, S. N.; Zhirov, V.; Zhirov, D.; Kabachii, Y. A.; Kochev, S. Y.; Valetsky, P. M.; Stein, B.; Kiseleva, O. I.; Polyakov, S. N.; Shtykova, E. V.; Nikulina, E. V.; Svergun, D. I.; Khokhlov, A. R. *J. Phys. Chem. B* **2005**, *109*, 18786–18798.
(61) Christodoulakis, K. E.; Vamvakaki, M. *Macromol. Symp.* **2010**, *291/292*, 106–114.
(62) Vamvakaki, M.; Palioura, D.; Spyros, A.; Armes, S. P.; Anastasiadis, S. H. *Macromolecules* **2006**, *39*, 5106–5112.
(63) Borsboom, M.; Bras, W.; Cerjak, I.; Detollenaere, D.; van Loon, D. G.; Goedtkindt, P.; Konijnenburg, M.; Lassing, P.; Levine, Y. K.; Munneke, B.; Oversluizen, M.; van Tol, R.; Vlieg, E. *J. Synchrotron Radiat.* **1998**, *5*, 518–520.

(64) Bras, W.; Dolbnya, I. P.; Detollenaere, D.; van Tol, R.; Malfois, M.; Greaves, G. N.; Ryan, A. J.; Heeley, E. *J. Appl. Crystallogr.* **2003**, *36*, 791–794.
(65) Gabriel, A.; Dauvergne, F. *Nucl. Instrum. Methods* **1982**, *201*, 223–224.
(66) *Neutron, X-rays and Light. Scattering Methods Applied to Soft Condensed Matter*; Zemb, T., Linder, P., Eds.; North-Holland: Amsterdam, 1999.
(67) Schaefer, D. W.; Martin, J. E.; Wiltzius, P.; Cannell, D. S. *Phys. Rev. Lett.* **1984**, *52*, 2371–2374.
(68) A shallow minimum appears at $q = 0.068$ nm$^{-1}$ and can be attributed to a second-order minimum of the form factor of a sphere of radius around 115 nm for the metallated microgel particles. This signifies that the incorporation of $K_2PtCl_6$ results in the deswelling of the microgel because of the ionic complexation between the divalent $PtCl_6^{2-}$ anions and the protonated tertiary amine groups of the polymer resulting in the formation of additional ionic "cross-links".[51]
(69) Glatter, O.; Kratky, O. *Small Angle X-ray Scattering*; Academic Press: New York, 1982.